Surface & Coatings Technology 400 (2020) 126245

Contents lists available at ScienceDirect

Surface & Coatings Technology

journal homepage: www.elsevier.com/locate/surfcoat

Deposition and oxidation behavior of atmospheric laminar plasma sprayed Mo coatings from 200 mm to 400 mm under 20 kW: Numerical and experimental analyses

Hui-Yu Zhang, Sen-Hui Liu, Chang-Jiu Li, Cheng-Xin Li*

State Key Laboratory for Mechanical Behavior of Materials, School of Materials Science and Engineering, Xi'an Jiaotong University, Xi'an, Shaanxi 710049, China

ARTICLE INFO

Keywords:
Laminar plasma spray
Mo coatings
Particle behavior
Microstructure
Hardness

ABSTRACT

A stable laminar plasma jet with a jet length of above 600 mm was adopted to deposit molybdenum coatings to investigate the behavior of high-melting point metal, molybdenum, and particles during laminar plasma spraying process. The temperature, velocity, and species distribution of the plasma jet were calculated by numerical simulation. In the experiment, the temperature and velocity distribution of the in-flight particles were measured, and the microstructure and properties of the coatings were analyzed. Combining the results of the simulation and experimental results, the deposition behavior and oxidation mechanism of the coatings prepared at the spray distance from 200 mm to 400 mm were discussed. The results indicate that both the laminar plasma jet and injected particles exhibit high temperature and low velocity, and low temperature and velocity gradients. The microstructure of the coatings shows a high similarity and hardly changes when the spray distance exceeds 250 mm. When the spray distance is 200 mm, post-deposition oxidation occurs due to the heating effect of the long plasma jet on the substrate. In contrast, when the spray distance is longer, the particles undergo severe in-flight oxidation, and the oxide formed is uniformly distributed in the coating improving the hardness from 500 $HV_{0.3}$ to 700 $HV_{0.3}$.

1. Introduction

Thermal spraying is a material surface technology that finds extensive application in various industries including the repair of damaged metal parts, preparation of structural coatings to prevent surface wear [1], protection of metal components from high-temperature erosion [2], and preparation of special functional coatings, such as hydrophobic coatings [3], fuel cell electrolytes, cathodes, and anodes [4–6]. Thermal spray deposition can occur, among other technologies, through the plasma spraying process where the spray material is injected into the plasma jet, heated to the point of melting, and accelerated to high velocities to impinge on the substrate and deposit a coating material. Compared to the flame, plasma has a higher temperature and velocity. Almost all materials with physical melting points can be melted by plasma jet indicating that plasma spray is suitable for spraying ceramics and high-melting-point metals.

Built on the structure of the turbulent plasma torch, the internal structure of the plasma torch has been properly adjusted in this work. To achieve a laminar plasma torch, segments and insulator rings are assembled to lengthen the channel of the plasma arc and increase the stability of arc voltage. Besides, a gas injection ring with 12 semicircular grooves circumferentially equispaced on its inner wall along the axial direction covers the tungsten cathode [7]. By decreasing the gas flow rate, the state of the plasma flow can be changed from turbulent to laminar, and the turbulent dissipation and the surrounding air entrainment in laminar plasma jet are minimized and therefore, the laminar plasma jet is longer, has a low noise, low velocity, temperature, and small temperature and velocity gradient [4,7,8]. During the laminar plasma spraying process, the velocity and temperature at the nozzle exit are lower than those of the traditional turbulent plasma jet. The temperature of the laminar plasma jet does not change significantly even on being propelled further from the nozzle exit. These characteristics increase the dwell time of particles in the plasma jet allowing them to be heated and melted completely even when the power is low. With laminar plasma jet also there is a high level of controllability of material processes such as surface quenching [9–11]. The latest research shows that during the laminar plasma spraying process, the average velocity of NiCrBSi particles is about 60 m/s and the average temperature is above 1800 °C [12]. In addition, the particle velocity and temperature can be maintained at a certain desired level within a

* Corresponding author.
E-mail address: licx@mail.xjtu.edu.cn (C.-X. Li).

https://doi.org/10.1016/j.surfcoat.2020.126245
Received 8 May 2020; Received in revised form 23 July 2020; Accepted 27 July 2020
Available online 29 July 2020

specified spraying distance due to the low temperature and velocity gradient.

Previous studies on laminar plasma spray have mainly focused on ceramic coatings [13–16]. However, the behavior of metal feedstock in the laminar plasma jet still remains unclear. Molybdenum is one of the most common high-melting-point metals with a melting point of approximately 2620 °C and therefore results to a good high-temperature performance. At present, molybdenum coatings are used extensively in automotive, aerospace, paper, and plastic industries [17]. This is possible because pure molybdenum coating and the molybdenum-based alloy coating oxidize during the wear process forming molybdenum oxide that acts as a solid lubricant that helps reduce the coefficient of friction. The high-hardness characteristic of the molybdenum oxide also enables it to exhibit excellent wear resistance. Generally, molybdenum coatings prepared by conventional atmospheric plasma spray process have superior wear and abrasion resistant characteristics than that those of flame-sprayed molybdenum coatings. By changing the plasma spray parameters, a dense molybdenum coating can be obtained using supersonic plasma spraying process [18] thereby providing extra protection of the substrate surfaces against abrasion.

However, due to the high melting point of molybdenum, the process parameters including the spray distance will affect the structure and properties of the coating to a large extent. This is because when the spray distance is too small, molybdenum particles are heated insufficiently and therefore cannot be melted completely. On the contrary, when the spray distance is too large, the molybdenum particles will solidify because of the decrease in temperature.

The purpose of this study is to investigate the behavior of high-melting-point metal particles in the laminar plasma jet and their behavior when deposited on the substrate surface. This study will also establish how these behaviors affect the structures and properties of the coatings. Numerical simulation is used to calculate the temperature, velocity, species distribution of the plasma jet, and the experimental method is used to investigate the flow characteristics of the injected particles, prepare the coatings, and determine the microstructure and mechanical properties of the coatings.

2. Materials and method

2.1. Simulation on plasma jet

A numerical simulation of the plasma jet is also carried out to model the spraying process. The composition of the plasma jet in this study is nitrogen-argon plasma with 70% nitrogen and 30% argon [13,19]. The simulation of the plasma jet is based on the following assumptions: (1) the plasma flow is laminar and quasi-steady; (2) the plasma jet operates in local thermal equilibrium (LTE) state and is optically thin to the extent that the radiation is negligible; (3) the heat and mass transfer properties of the plasma jet are temperature-dependent; (4) the electric field near the nozzle exit is negligible; (5) the terms of the viscous dissipation and pressure work in the energy equation are negligible due to the small Mach number; (6) the properties of the mixture of ambient air and plasma gas follow the volume mixing law.

The basic governing equations for the continuity, momentum, energy of the plasma can be written as follows:

Continuity equation:

$$\frac{1}{r}\frac{\partial}{\partial r}(r\rho v_r)+\frac{1}{r}\frac{\partial}{\partial\theta}(\rho v_\theta)+\frac{\partial}{\partial z}(\rho v_z)=0$$

Momentum conservation equations:

$$\frac{1}{r}\frac{\partial}{\partial r}(r\rho v_r^2)+\frac{1}{r}\frac{\partial}{\partial\theta}(\rho v_r v_\theta)+\frac{\partial}{\partial z}(\rho v_r v_z)$$
$$=-\frac{\partial p}{\partial r}+\frac{\partial}{\partial r}\left(2\mu\frac{\partial v_r}{\partial r}\right)+\frac{1}{r}\frac{\partial}{\partial\theta}\left[\mu\left(\frac{1}{r}\frac{\partial v_r}{\partial\theta}+\frac{\partial v_\theta}{\partial r}-\frac{v_\theta}{r}\right)\right]+\frac{\partial}{\partial z}$$
$$\left[\mu\left(\frac{\partial v_r}{\partial z}+\frac{\partial v_z}{\partial r}\right)\right]+\frac{2\mu}{r}\left(\frac{\partial v_r}{\partial r}-\frac{1}{r}\frac{\partial v_\theta}{\partial\theta}-\frac{v_r}{r}\right)+\rho\frac{v_\theta^2}{r}$$

$$\frac{1}{r}\frac{\partial}{\partial r}(r\rho v_r v_\theta)+\frac{1}{r}\frac{\partial}{\partial\theta}(\rho v_\theta^2)+\frac{\partial}{\partial z}(\rho v_\theta v_z)$$
$$=-\frac{1}{r}\frac{\partial p}{\partial\theta}+\frac{\partial}{\partial r}\left[\mu\left(\frac{\partial v_\theta}{\partial r}-\frac{v_\theta}{r}+\frac{1}{r}\frac{\partial v_r}{\partial\theta}\right)\right]+\frac{1}{r}\frac{\partial}{\partial\theta}$$
$$\left[2\mu\left(\frac{1}{r}\frac{\partial v_\theta}{\partial\theta}+\frac{v_r}{r}\right)\right]+\frac{\partial}{\partial z}\left[\mu\left(\frac{\partial v_\theta}{\partial z}+\frac{1}{r}\frac{\partial v_z}{\partial\theta}\right)\right]+\frac{2\mu}{r}$$
$$\left(\frac{1}{r}\frac{\partial v_r}{\partial\theta}+\frac{\partial v_\theta}{\partial r}-\frac{v_\theta}{r}\right)-\rho\frac{v_r v_\theta}{r}$$

$$\rho\frac{1}{r}\frac{\partial}{\partial r}(r\rho v_r v_z)+\frac{1}{r}\frac{\partial}{\partial\theta}(\rho v_z v_\theta)+\frac{\partial}{\partial z}(\rho v_z^2)$$
$$=-\frac{\partial p}{\partial z}+\frac{1}{r}\frac{\partial}{\partial r}\left[\mu r\left(\frac{\partial v_r}{\partial z}+\frac{\partial v_z}{\partial r}\right)\right]+\frac{1}{r}\frac{\partial}{\partial\theta}\left[\mu\left(\frac{\partial v_\theta}{\partial z}+\frac{1}{r}\frac{\partial v_z}{\partial\theta}\right)\right]+\frac{\partial}{\partial z}$$
$$\left(2\mu\frac{\partial v_z}{\partial z}\right)$$

Energy conservation equations:

$$\frac{\partial(\rho uh)}{\partial z}+\frac{1}{r}\frac{\partial(r\rho vh)}{\partial r}$$
$$=\frac{\partial}{\partial z}\left[\left(\frac{k}{C_p}+\frac{\mu_T}{\sigma_h}\right)\frac{\partial h}{\partial z}\right]+\frac{1}{r}\frac{\partial}{\partial r}\left[r\left(\frac{k}{C_p}+\frac{\mu_T}{\sigma_h}\right)\frac{\partial h}{\partial r}\right]-U_r-\frac{\partial}{\partial z}$$
$$[(h_A-h_B)J_z]-\frac{1}{r}\frac{\partial}{\partial r}[r(h_A-h_B)J_r]-\frac{\partial}{\partial z}\left[\frac{k}{c_p}(h_A-h_B)\frac{\partial f_A}{\partial z}\right]-\frac{1}{r}\frac{\partial}{\partial r}$$
$$\left[\frac{k}{c_p}(h_A-h_B)\frac{\partial f_A}{\partial r}\right]+u\frac{\partial p}{\partial z}+v\frac{\partial p}{\partial r}+(\mu+\mu_T)$$
$$\left\{2\left[\left(\frac{\partial u}{\partial z}\right)^2+\left(\frac{\partial v}{\partial r}\right)^2+\left(\frac{v}{r}\right)^2\right]+\left(\frac{\partial u}{\partial r}+\frac{\partial v}{\partial z}\right)^2\right\}$$

u - the axial velocity;
v - the radial velocity;
ρ - the temperature-dependent density of the plasma gas;
μ - the viscosity;
k - the thermal conductivity;
C_p - the specific heat at constant pressure;
h - the temperature-dependent specific enthalpy;
U_r - the energy of radiation;
P – the static pressure.

A long cylindrical flow field and structure cells were accustomed. The schematic of the mesh is illustrated in Fig. 1. Line AB represents the inlet of the nitrogen-argon plasma gas. Line BC represents the water-

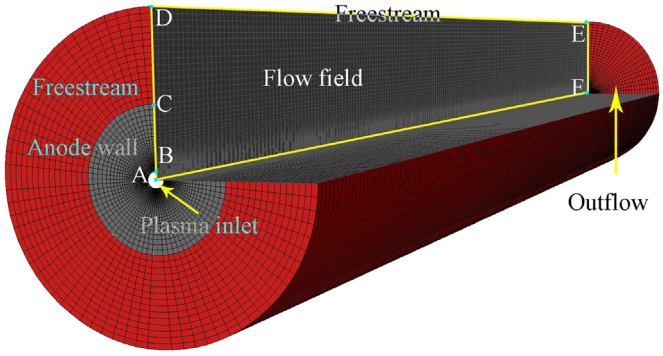

Fig. 1. Computational domain on r–z section.

Table 1
Boundary conditions of the computational domain.

Defined condition	Boundary	Temperature (K)	Velocity (m/s)	Length (mm)
Plasma inlet	AB	Fig. 2	Fig. 2	2.5
Anode wall	BC	$h_w(T - T_w)$	–	22.5
Freestream	CD	300	–	25
Freestream	DE	300	–	700
Out flow	EF	–	–	50

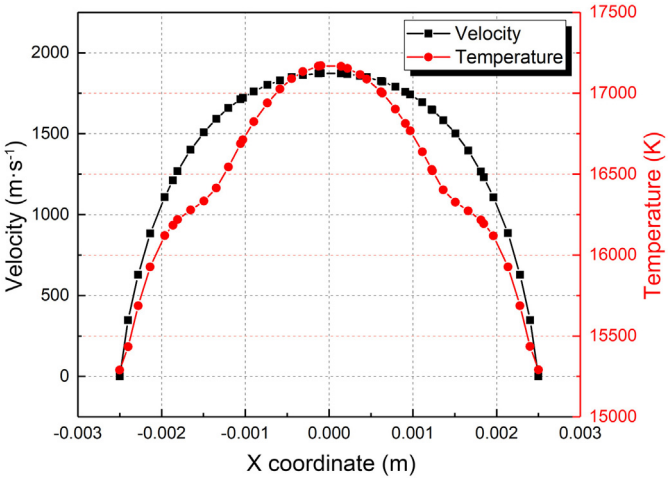

Fig. 2. Boundary conditions at the nozzle exit: velocity and temperature.

cooling plasma torch anode for which the thermal boundary conditions are specified by a heat transfer coefficient (h_w) of 1.0×10^5 W·m^{-2}·K^{-1} and reference cooling water temperature (T_w) of 300 K. The polyline CDEF represents the free boundary adjacent to the atmospheric environment. Line AF is the z-axis that is the center line of the whole simulation domain. The details of boundary conditions are given in Table. 1 based on the previous report and shown in Fig. 2 [19].

2.2. Formation of atmospheric laminar plasma sprayed Mo coatings

The powder used in the experiment was a commercial high-density molybdenum powder (MA 9900); 150–300 mesh with irregular shape. The substrates used in the experiment are 304 stainless steel disks with diameter of 25.5 mm and thickness of 2 mm. Before the spraying process, the substrates were sand blasted and preheated to 150 °C. A custom-made powder feeder based on gravity was used in this study. A laminar plasma torch with the custom-made powder feeder was set up on a welding robot. The moving plane was aligned parallel to the substrate which was perpendicular to the ground. The moving path was positioned in the vertical direction and provision was made for the gradual forward movement in the horizontal direction. Details on the spraying process are given in Table. 2. The single splats were deposited on the polished 304 stainless steel with a vertical traverse speed of 1000 mm/s.

Table 2
Parameters of spraying process.

Spray parameter	Value
Current (A)	140
Voltage (V)	142
Gas flow rate (L·min^{-1})	9.5
Mixture ratio (N_2:Ar)	7:3
Vertical traverse speed (mm·s^{-1})	400
Horizontal pitch distance (mm)	4
Spray distance (mm)	200, 250, 300, 350, 400
Powder feed rate (g·min^{-1})	10.58

Before spraying the coatings, the temperature and velocity of the inflight particles at different positions were detected. The acquisition positions along the axis direction are the same as the substrate positions. At each position, 2000 particles were measured. As-sprayed coatings were marked from A to E depending on the spray distance. An X-ray diffractometer (PANalytical, X'Pert PRO) was used to identify the phases, analysing the surface of coatings. The surface morphologies, fractures, and polished cross-sections of the coatings were analyzed using scanning electron microscopy (TESCAN, MIRA 3 LMH). Before observation, samples were cleaned ultrasonically. The surface of the samples was observed under the magnification of 100× and 500× using secondary electrons. Samples for cross sectional observation were cut perpendicular to surface, and ground by sandpaper from 80 mesh to 2000 mesh, then polished by rotary buffer (CVOK, MP-2). The polished cross sections were observed using backscattered electrons under magnification of 200×. The fractures were prepared by breaking the coating after the substrates were ground to thin films and immersed in liquid nitrogen. The magnification of fracture views is 10,000×. The surface roughness was determined using three-dimensional (3D) laser confocal microscope (Keyence, VK-X1000). The porosity characterization of the coating was done by image analysis using at least ten SEM photos of polished cross section. The Vickers hardness was also analyzed to assess the fundamental mechanical properties of the coatings using a BUEHLER, MICROMET5104 equipment with a loading of 0.3 kgf for 30 s.

3. Results and discussions

3.1. Simulation of plasma jet

In this study, laminar plasma jet is stabilized and the length is found to exceed 600 mm. Turbulent fluctuations are only observed at the far end of the plasma jet, while the central region is relatively stable as shown in Fig. 3(a). At the same time, the plasma jet is curved indicating a slight rising tendency. This is attributed to the low density of plasma and the buoyancy of air.

Detailed information on the temperature distribution, velocity of the plasma jet and mass fraction of the nitrogen-argon mixture plasma gas on different planes are shown in Fig. 3(b)–(f). When the spray distance is short, the diameter of the high-temperature area is relatively large. As the spray distance increases, the diameter of the high-temperature area decreases gradually. At the same time, the low-temperature zone of the plasma expands gradually, and the overall width of the plasma becomes larger. A slight lifting tendency is also observed as shown in Fig. 3(f) which represents the shape of the plasma jet. The overall profile of the plasma jet is illustrated in Fig. 3(g) where the upper part represents the temperature distribution and the lower part represents the velocity distribution. The calculated temperature distribution and the brightness of the actual plasma jet also demonstrate a high consistency since both of them increase at the tail of the plasma jet.

On examining the 200-mm cross-section of the central region, the mass fraction of nitrogen and argon mixture plasma gas is 72%. In contrast, on examining the 400-mm cross-section of the central region, the content of the plasma gas is 52%. During flight, spray particles are under oxidation which mainly depends on the oxygen content. Therefore, when the air mass fraction is 28%, the oxygen content is approximately 5.8%, and when the air content is 48%, the oxygen content is approximately 10%.

On examining the central axis of the plasma jet, the temperature shows a significant decrease near the nozzle exit from 17,200 K to 7000 K in a spray distance of about 90 mm. However, when the distance exceeded 90 mm, the temperature gradient decreased. At the plasma torch exit (within 90 mm), where there is an expansion, the temperature decrease process shows a slightly fast-slow-fast tendency.

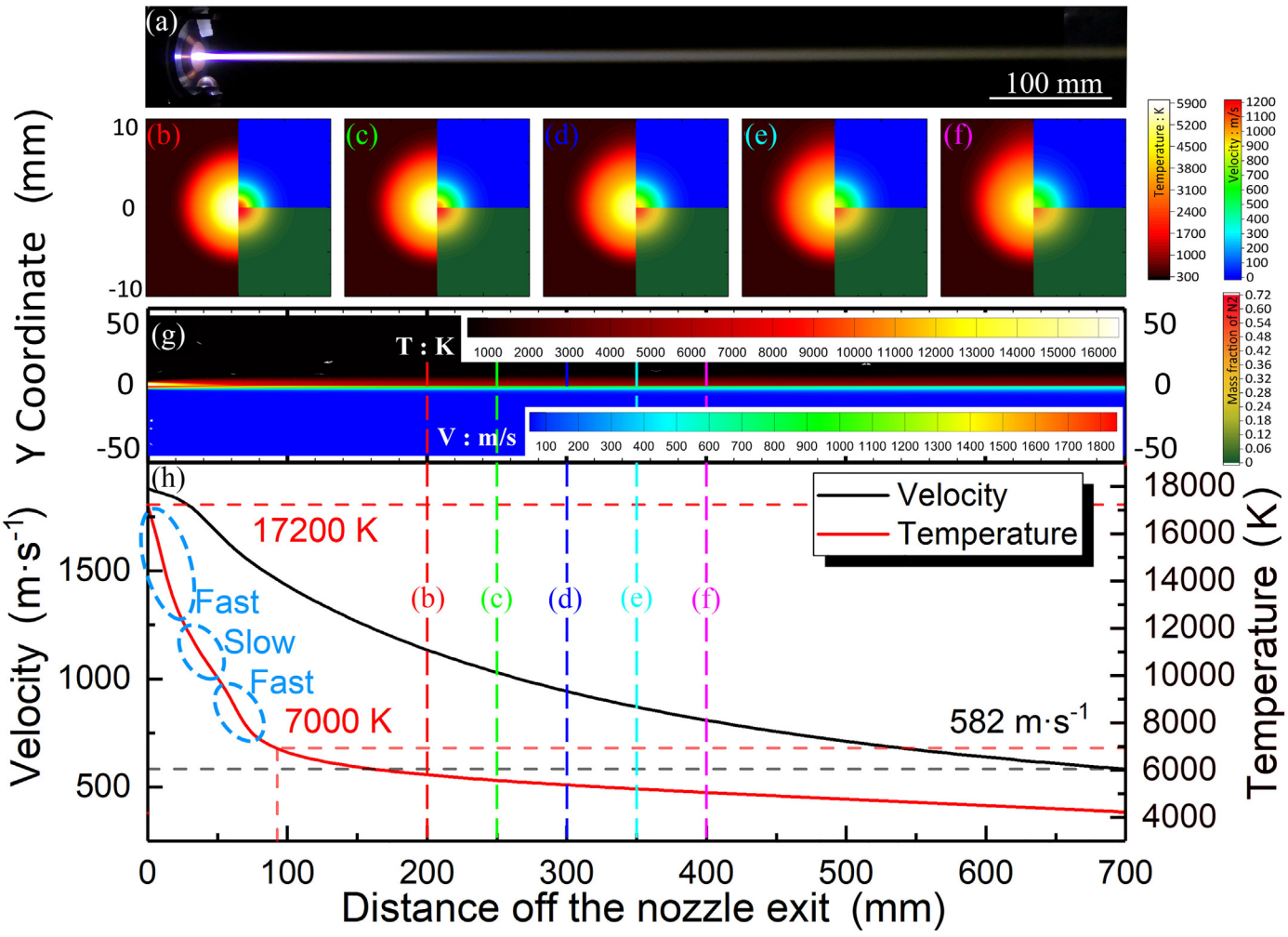

Fig. 3. (a) The appearance of laminar plasma jet and simulation results on the laminar plasma jet: (b) temperature (left),velocity (upper right) and mass fraction (lower right) of plasma gas on the plane 200 mm off the nozzle exit, (c) 250 mm, (d) 300 mm, (e) 350 mm, (f) 400 mm, (g) temperature (upper) and velocity(lower) distribution of the plasma jet, (h) the temperature and velocity of the center line of the plasma jet along Z axis.

This gradient fluctuation was attributed to the non-linear thermal conductivity and specific heat capacity change with temperature. After a slight fluctuation, the temperature gradient of the plasma jet stabilizes at approximately 3.9 K/mm, which is significantly less than that of the turbulent plasma jet. The velocity of the plasma jet steadily decreases, and the gradient slightly changes with the distance. During this experiment, the velocity gradient is approximately 1.6 (m/s)/mm within the spray distance and the minimum velocity is 582 m/s at the end of the calculated domain.

The simulation results of temperature and velocity might be slightly higher than the experimental results because the turbulent dissipation is neglected in the laminar flow model. However, the general trends of both temperature and velocity are in agreement with previous reports [9].

The fluid flow is characterized by the Reynolds (*Re*) number. When the *Re* number is small, the flow state is considered to be laminar. *Re* number is expressed as the ratio between the inertial forces in a fluid and the viscous forces and is represented by the following equation:

$$Re = \frac{\rho v d}{\mu}, \quad (1)$$

where ρ represents the density of the plasma gas; *v* represents the velocity of the plasma; *d* represent the characteristic length; and μ represents the viscosity of the plasma.

In addition to being dependent on the density and viscosity, the Re number also depends on the velocity and diameter of the plasma jet. Since density and viscosity are regarded as the function of temperature, the most important factors affecting the *Re* number are the temperature and velocity.

As the ambient environment remains constant when plasma jet exits the nozzle, the most critical factor is the state at the nozzle besides the structural difference between the plasma torches. Generally, a larger *Re* number indicates a high level of turbulence. When *Re* number $<$ 2000, the flow state can be considered as laminar flow. For the laminar plasma jet, the velocity at the nozzle is relatively lower than that of the turbulent plasma jet due to the low gas flow rate. From the simulation results, the laminar plasma jet shows a relatively low *Re* number of approximately 1400 (calculated based on the average mechanical properties and velocity), at the nozzle exit.

3.2. Components of the coatings

Coatings are marked based on the spray distance as A, B, C, D, and E. Here, A is obtained at the 200 mm while E is obtained at 400 mm. The X-ray diffraction (XRD) patterns of all the samples and the powder indicate that oxidation occurred during the spray process (Fig. 4). Besides the four characteristic peaks of (110), (200), (211), and (220) plane of molybdenum, a few peaks representing molybdenum oxide are also present. For sample B, C, D, and E, the main oxide phase consists of tugarinovite, which is a monoclinic molybdenum dioxide. High-

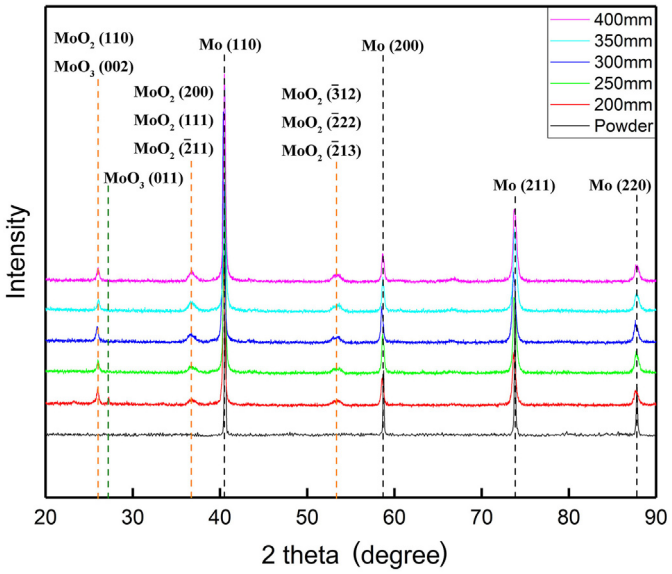

Fig. 4. XRD patterns of coatings and original powder.

intensity peaks of tugarinovite appear at about 26°, 36°, and 53°, which are in good agreement with the XRD patterns. For sample A, which is obtained from the nearest spray distance, a special inconspicuous peak appears at approximately 27°. This could be the peak of orthorhombic molybdite, molybdenum trioxide (210) plane, or monoclinic molybdenum trioxide (011) plane.

The flow state results of the plasma jet demonstrate two main differences between the turbulent plasma jet and laminar plasma jet: velocity and length. During the spraying process, a long laminar plasma jet makes it possible to achieve coatings at a longer distance. However, a laminar flow still causes the entrainment of ambient air as shown in the calculated mass fraction distribution of the laminar plasma jet (Fig. 3). A long flight distance and low velocity of particles increases the reaction time of in-flight particles with the engulfed air leading to oxidation. This oxidation reaction during flight consequently leads to the formation of molybdenum dioxide.

A schematic diagram of the oxidation reaction during laminar plasma spray is shown in Fig. 5(a). When injected into the plasma jet, particles melt into droplets. Based on the flow state inside the droplets and the mass transport, these droplet can be divided into two types [20–22]: the first one is a diffusion-dominated droplets where the liquid phase in the droplet is relatively stationary and oxygen is transported to the core by diffusion; the second one is a convection-dominated droplet where the liquid phase in the droplet flows fast forming the Hill's spherical vortex and oxygen is transported to the core by convection [6,21]. Based on the results of the elemental analysis of the cross-section of the coatings (Fig. 5b,c), after the reaction with liquid molybdenum on the surface of the diffusion-dominated droplet and the generation of a thin molybdenum dioxide film, oxygen continues to react with fresh molybdenum inside the droplet by diffusion rather than reacting with MoO_2 to generate MoO_3. For the convection-dominated droplets, fresh liquid molybdenum continuously flows to the surface of the droplet reacting with oxygen generating molybdenum dioxide. Therefore, when the spray distance is long, in-flight particles are more likely to undergo oxidation reaction which generate MoO_2. Even if a small amount of MoO_3 is generated during the flight due to the high temperature and oxygen partial pressure, volatile MoO_3 may mostly evaporate, barely influencing the XRD result.

Besides the in-flight oxidation, post-deposition oxidation can also occur [23]. When the spray distance is short (approximately 200 mm), the laminar plasma jet can reach the surface of the substrate and heat the substrate to high temperature [18]. Immediately after the droplet gets sufficiently flattened on the substrate, the temperature will remain higher than 350 °C, making it possible for post-deposition oxidation to take place. After the solidification of droplets, oxygen is not able to penetrate to the inner part and react with molybdenum fast to continuously generate molybdenum dioxide. Therefore, the formation of molybdenum trioxide occurs on the surface as a result of post-deposition oxidation as shown in Fig. 5(d). For the coatings sprayed with a longer spraying distance, the already deposited particles are not close enough to be covered by the laminar plasma jet and form molybdenum trioxide. The main product of the oxidation reaction is generated from the in-flight oxidation. During the flight, when the particle has melted, the oxygen will be transported to the core of particles for the active liquid phase by diffusion or convection and this prevents the formation of molybdenum trioxide. Therefore, the coatings sprayed with a longer spraying distance demonstrate a high consistency and the peak for molybdenum trioxide is absent in the XRD patterns.

3.3. Particle behavior

An increase in the length and a decrease in velocity increase the dwelling time of the particles in the plasma jet, which facilitates the heating of the particles from solid to liquid form. Once particles are injected into laminar plasma jet during the spray process, the length of the plasma jet decreases since particles absorb the heat in order to be melted. However, the distance of the high-temperature region of laminar plasma jet is still long.

The temperature and velocity of the in-flight particles and the morphology of single splats are analyzed to explain the deposition behavior of the particles. The average temperature and velocity of the in-flight particles are analyzed using the DPV-2000 system. Both temperature and velocity decrease with the spray distance. The average temperature of the particles decreases from 2840 °C to 2334 °C and the average velocity of the particles decreases from 92 m/s to 49 m/s (Fig. 6).

The melting point of molybdenum is approximately 2620 °C, which is slightly higher than the temperature at which the particle is detected on the plane 300 mm away from the plasma torch and beyond. However, the DPV-2000 system can only measure the temperature at the particle surface. The temperature of the core of the particle might still be high. As mentioned before, particles react with oxygen during the long flight distance. During the experiment, the surface of the molybdenum droplets is at high temperature and produces a thin film of volatile molybdenum oxide which decreases the surface temperature drastically. The melting point of particles with different oxygen content is described in the Mo-O binary phase diagram (Fig. 6). The melting point decreases with the mass fraction of oxygen. From the results of the XRD pattern, the oxidation products mostly consist of MoO_2. The lowest temperature of Mo–MoO_2 alloy is approximately 2150 °C, which is lower than the average temperature of the particles from the farthest plasma jet position in the experiment. Therefore, these particles maintain their liquid state and the actual temperature is high. Therefore, the decrease of average temperature does not affect the deposition. When the spray distance is long, the particles are still under a high temperature that is above the local melting point and remain in molten state.

Theoretically, in the laminar plasma jet, particles tend to maintain their molten state because the long distance high-temperature region increases the dwell time and delays the solidification process and within a certain range of distance, the condition of the particles from different planes tends to remain similar to each other.

To investigate the actual melting conditions of the particles, single splats are obtained at different planes along the direction of spray on a polished stainless-steel substrate. Typical semi-melted particles, splashed splats (well melted) and fragmented splats (melted and of high temperature), are found at all the spray distances. A general view of the single splats obtained at 300 mm is shown in Fig. 7(a). During the

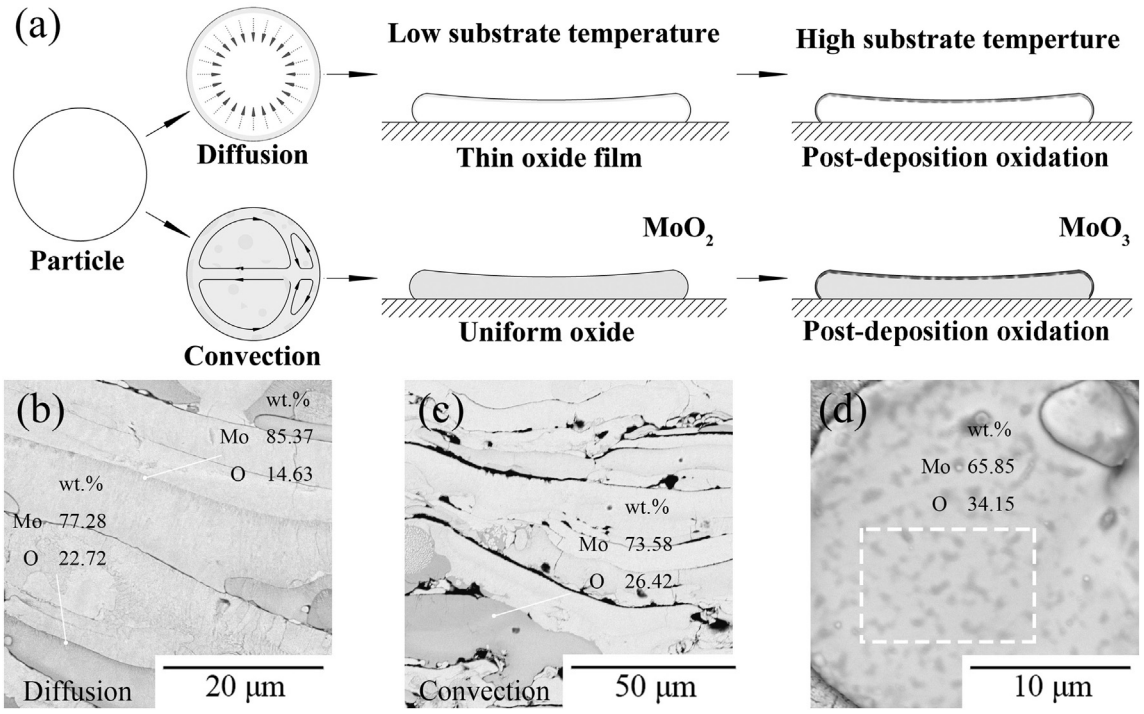

Fig. 5. (a) Schematic diagram of oxidation history of molybdenum particle in laminar plasma jet, (b) element analysis on diffusion-dominated splats, (c) element analysis on convection-dominated splats, and (d) element analysis on surface of sample A.

spraying process, some particles do not enter the center of the plasma jet and are not heated enough to the point of completely melting and are finally deposited as shown in Fig. 7(b). Both the gas absorbed by the in-flight droplets and the substrate contributed to the deposition behavior of the particles by causing splashes as shown in Fig. 7(c) and (d) preventing the heat transfer from heated particles to substrate [24]. Most completely melted particles have been subjected to high temperatures that are significantly higher than the melting point of the substrate. When impinged on the polished substrate, the molybdenum droplets solidify fast and float on the local melted substrate. When the temperature of both the substrate and the molybdenum splat are decreased, the splat splits into fragments (Fig. 7e) due to the high strength of bonding of the welded part between the periphery of the splat and the substrate [25].

Considering both slightly splashed splats and severely splashed splats as splashed splats, the amount of all these three types of single splats is counted to investigate the difference between distinct spray distances. At each position, more than 200 single splats were collected

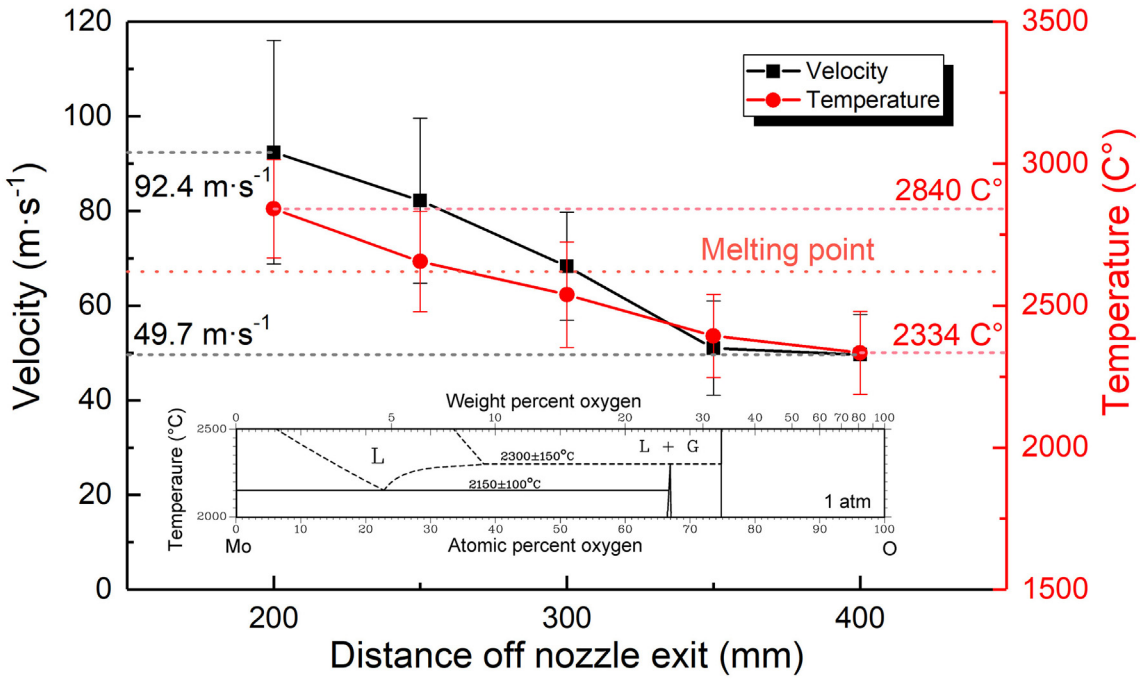

Fig. 6. Temperature and velocity of in-flight particles in laminar plasma spray and part of the Mo - O binary phase diagram.

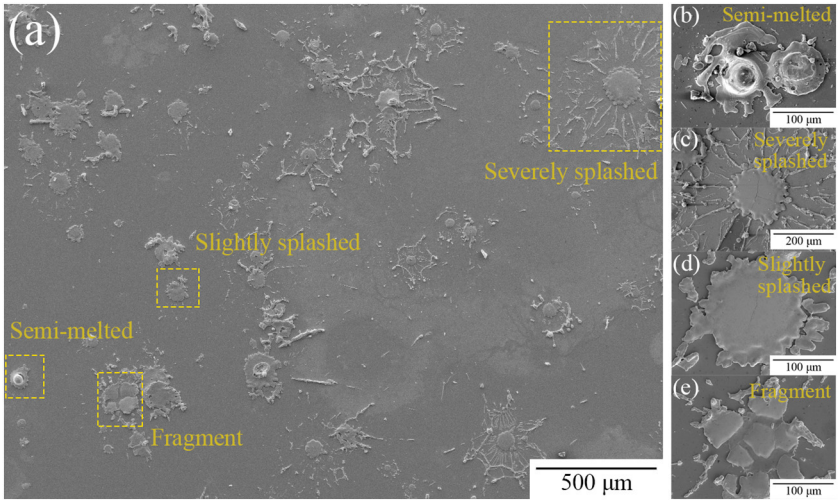

Fig. 7. (a) General view of single splats obtained at spray distance of 300 mm and four typical morphologies of single splats (b) semi-melted, (c) severely splashed, (d) slightly splashed, (e) Fragmented.

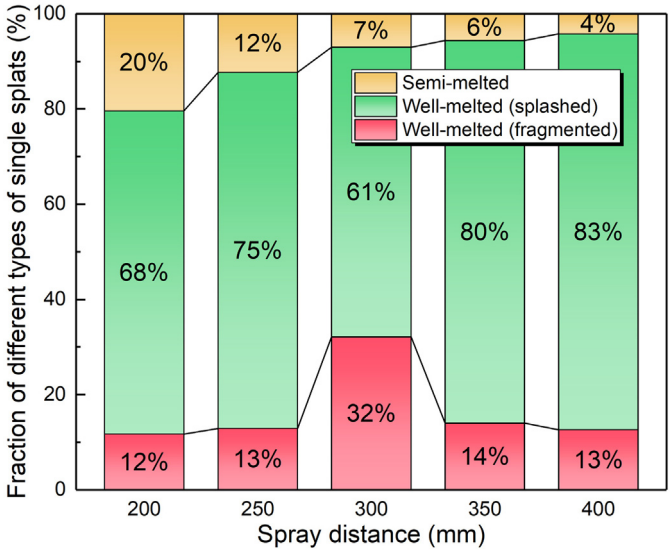

Fig. 8. Fractions of different types of particles at different spray distance.

and the statistical results are shown in Fig. 8.

When the spray distance is short, even though the temperature of the particles is high, the amount of semi-melted particles is also more than at other positions. As mentioned before, the temperature captured by DPV-2000 is the temperature of the particle surface. Therefore, the core of the particles may not be heated to total melting. When the spray distance increases, the heating process lasts longer, which provides for fully melted particles. Therefore, even though the surface temperature decreases, the fraction of semi-melted particles is reduced when the spray distance increases. It can be also inferred from the statistic result of different types of single splats that the number of the high-temperature fragmented splats reaches the highest fraction, about 32%, and begins to decrease due to the temperature drop which is attributed to the evaporation of the volatile MoO_3.

3.4. Structures of coatings

Surface morphologies of each sample were observed using the 3D-laser confocal microscope. For each sample, five uniformly distributed points on the surface were examined. From the morphological information captured, protrusions on sample A are conspicuous and of largest amount, which is consistent with the surface roughness (Fig. 9).

The results of surface roughness of molybdenum coatings indicate a decreasing trend with spray distance. The surface roughness of sample A is approximately 18% higher than that of the other samples. This observation agrees with those of previous reports on laminar plasma sprayed coatings, where massive island-like protrusions were reported on the surface of coatings sprayed with a short spraying distance [14,15].

The structures of coatings obtained at different spray distances are similar. This tolerance with long spray distances is attributed to the low velocity and temperature gradient of the laminar flow of the plasma jet [9,26]. The temperature and velocity of laminar plasma jet decrease slowly making the particles to retain their physical state at different positions along the direction of spray. Therefore, a high uniformity of the coating structure is maintained confirming the distance tolerance of the laminar plasma spraying process.

Scanning electron microscopy (SEM) images of surfaces of the coatings indicate that the high surface roughness of sample A is due to the evenly distributed protrusions (Fig. 10, first image on first line). This may be attributed to the particles which have not been melted due to presence of insufficient heat on the periphery of the laminar plasma jet and the splashes generated by particles with large *Re* numbers [27]. Generally, unmelted particles form the “seeds” of the protrusions, and then the small particles, generated by splashes, gather surrounding the “seeds” to make the protrusions grow larger.

Laminar plasma jet has a lower temperature and velocity near the nozzle exit compared to the turbulent plasma jet. During the laminar plasma spraying process, particles are injected into the plasma jet by gravity. Some particles are not able to enter the center of the plasma jet where they can be heated to complete the melting process and are only melted partially. When the partially melted particles are deposited on the substrate, the “seeds” of protrusions are formed. According to the statistical result of single splats, when the spray distance increases, the fraction of the partially melted particles decreases. Therefore, more “seeds” of the protrusion are formed when the spray distance is 200 mm. When the spray distance is longer, the expansion of the plasma jet helps to heat the particles around the plasma jet reducing the fraction of partially melted particles. Besides, some low-temperature particles, which are not heated well or solidified, rebound on the coating surface and are not able to be deposited. Consequently, when the spray distance is long, fewer “seeds” of protrusions are formed.

Low-power laminar plasma sprayed molybdenum coatings have a lamellar structure. The porosity of the coating is about 22% when the spray distance is 200 mm, and decreases to approximately 11% when

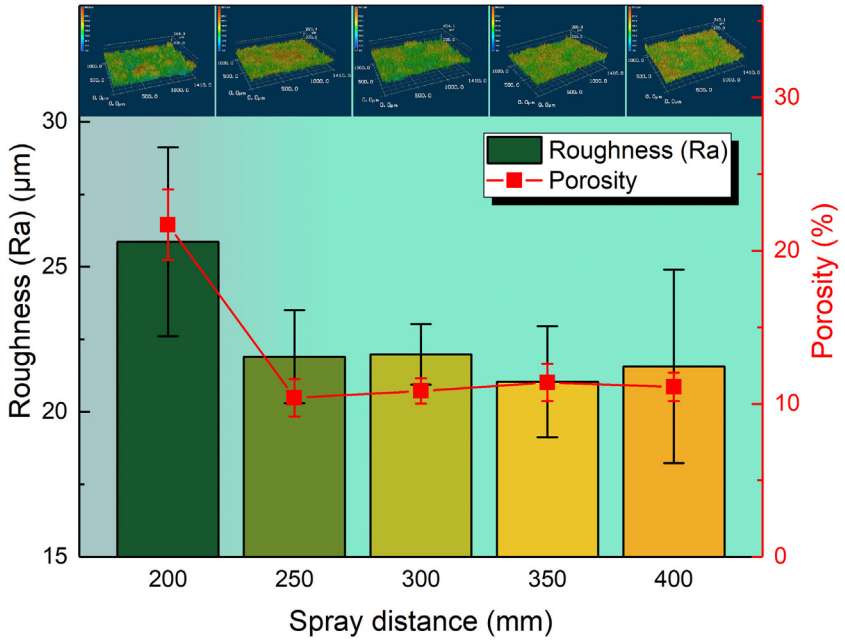

Fig. 9. Surface roughness and porosity of coatings.

the spray distance is 250 mm and above. This phenomenon indicates that the protrusions on a deposited layer might be the reason for high porosity.

As mentioned before, the velocity of the particles at the standoff distance of 200 mm is the highest among all the distances. The average particle temperature decreases from 2840 °C to 2334 °C, about 17.7%. The average particle velocity decreased from 92.4 m/s to 49.7 m/s, about 45.3%. Both temperature and velocity influence the *Re* number of the particles. While the velocity influences the value directly, the temperature also influences the value by influencing the properties including viscosity and density. However, considering the temperature and velocity gradients and the effect of the temperature on the properties, the velocity decrease leads to *Re* decrease directly, while the temperature decrease will lead to the viscosity increase and density decrease to influence *Re*. Comparing the effect of these parameters, the influence of density changes on *Re* is negligible. Therefore, the *Re*

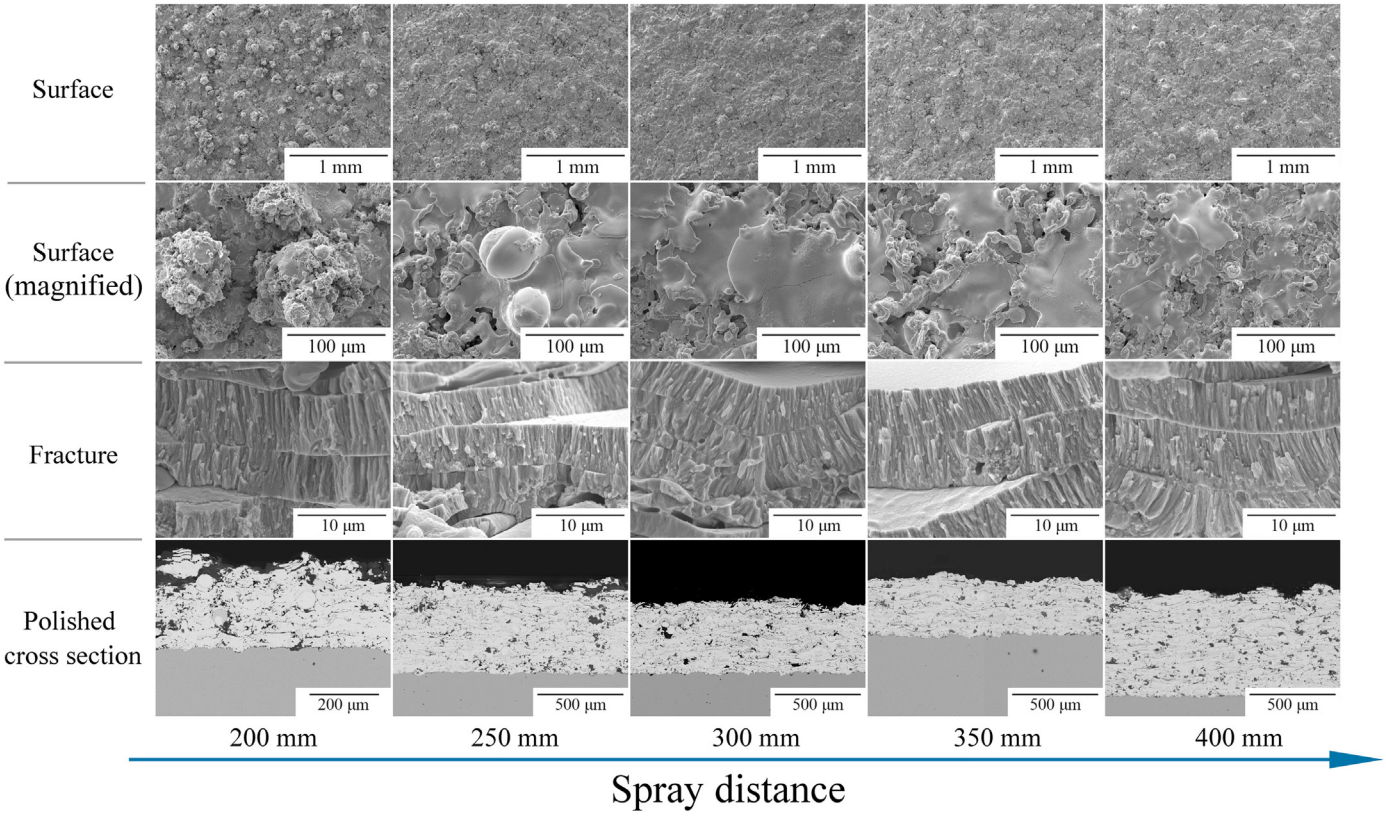

Fig. 10. SEM images of laminar plasma sprayed coatings.

number decreases with the standoff distance. Generally, particles with large *Re* numbers may cause severe splashes which contribute to the formation of protrusions. On the other hand, the substrate temperature also plays an important role on the formation of protrusions. When the standoff distance is short, the substrate is simultaneously heated by the long laminar plasma jet. When the substrate temperature increases, the vapor deposition process is enhanced. As the oxygen partial pressure is low, the oxidation process still occurs when the temperature is high enough to generate volatile MoO_3. Then the MoO_3 might evaporate and deposit or be adsorbed on the coating surface. Different from the PS-PVD process, this vapor deposition structure is a porous furry-like structure which has been proved to be hydrophobic [3], hindering the flattening process of the later impinging particles on the protrusions. Unable to be covered by later particles, the protrusion will gradually grow larger. Besides, the high substrate temperature would lead to the slow solidification of the particles, which also enhances the splashing process [28] to provide small particles gathering around the protrusions. When the spray distance is longer, the substrate temperature is below 200 °C, and most evaporated MoO_3 diffused to the atmosphere instead of depositing or being adsorbed on the coating surface. Therefore, most protrusions will be covered by later particles before they grow larger when the spray distance is long.

From the fracture view of each sample obtained at different spray distances (Fig. 10, third line), it can be concluded that at all the distances, the laminar plasma jet is able to heat the molybdenum particles to molten state. No significant difference is observed between the fractures of laminar plasma spray coatings and the counterpart of traditional plasma spray coatings indicating that the deposition process of laminar plasma spray process is similar to traditional plasma spray process and therefore, they could be used interchangeably.

All samples demonstrate a conspicuous lamellar structure, which is formed by flattened splats with a few partially melted and unmelted particles. Spray coatings show a discernible boundary between splats like ceramic coatings [29,30]. The fraction of partially melted particles slightly decreases with the spray distance. Because the temperature gradient of the laminar plasma jet is low, the high-temperature zone is long. Therefore, even when the spray distance is long, the duration of the heating process is increased. As a result, coatings obtained at longer spray distances show fewer unmelted particles compared to those of the coatings obtained from shorter distances.

Therefore, by combining the surface morphologies and the cross-sectional structures observed, it can be concluded that the structure of laminar plasma sprayed molybdenum coatings is insensitive to the spray distance for a certain range of distance.

3.5. Hardness of coatings

In general, the hardness of a coating is dependent on the property of the material and the structure of the coating. The findings of the hardness and oxygen content characteristics of the coating are shown in Fig. 11. When the spray distance reaches 300 mm, the hardness of the coating increases significantly from 520 $HV_{0.3}$ to 700 $HV_{0.3}$. When comparing with molybdenum coatings obtained by other spraying methods, laminar plasma sprayed coatings demonstrate equal hardness to that of traditional plasma sprayed pure molybdenum coatings [16] when the spray distance is short. In contrast, laminar plasma sprayed coatings demonstrate a high hardness similar to that of electro-thermal deposited coatings [31] when the spray distance is longer. According to the findings of the porosity of the coatings, the significant improvement of hardness might be attributed to the change of coating composition, mainly. Therefore, an assumption can be proposed that uniform molybdenum oxide results in the high hardness.

The oxide amount of each coating is measured by image analysis method to investigate the distribution of the molybdenum oxide. The areas where the oxygen concentration by EDS is at least 5 wt% (the concentration of O to form Mo-MoO_2 eutectic) identified, and the

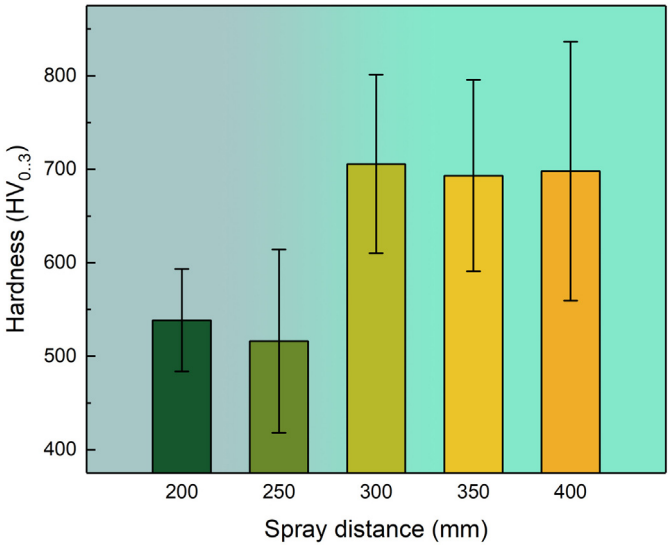

Fig. 11. Hardness of coatings.

greyscale contrast level of these areas in backscattered electron SEM images are taken to be the threshold level. Then the image analysis is performed on the same images to tell areas above and below this threshold, assuming that everything which has a darker contrast than the threshold is an oxide inclusion. The results of oxygen content show consistency with the results of hardness. When the oxygen content is lower, hardness is also lower. The oxide distribution measured by image analysis method (supplementary files) indicates the short distance sprayed coatings underwent less severe oxidation than long distance sprayed coatings and hence exhibited fewer oxide inclusions. Besides, when the spray distance is short, the oxide inclusions tend to concentrate in a minority of the particles, which also indicated that a uniform oxide distribution helps to enhance the hardness.

During laminar plasma spraying process, both in-flight oxidation and post-deposition oxidation occurs. From the XRD results, short distance spray coatings might undergo severe post-deposition oxidation. However, post-deposition oxidation only occurs on the surface, which can be found on the interface between layers and may not influence the hardness on a large scale. Therefore, the in-flight oxidation which provide oxidized particles to form more uniform mixed structure of metal and oxide is the main factor of the coating hardness.

Generally, longer dwelling time in the plasma jet leads to more in-flight oxidation, and the content of oxide is the key factor of hardness. According to the results for temperature and velocity distribution of particle captured by the DPV-2000 system, the temperature of molybdenum particles reaches the melting point and the particles are melted completely when the spray distance is short. Combined with the simulation results of oxygen partial pressure, it can be concluded that the degree of reaction between molybdenum particles and oxygen is small. Therefore, uniformly distributed oxides in the short distance sprayed coatings are few and therefore cannot significantly improve the hardness. In addition, coating A, obtained at 200 mm off the nozzle exit, experiences an enhancement from the plasma jet [10,11,32], which promotes interlamellar diffusion and improves cohesion. This might make coating A a little harder than coating B.

When the spray distance is long, the temperature and the velocity of the particles decrease, and the oxygen content of the jet increases. As a result, the probability of particles coming into contact with oxygen is increased and the dwell time is also increased. Under these conditions, high-temperature particles will melt off the nozzle exit and become oxidized and the medium-temperature particles will react with oxygen to form low-melting oxides on surface and then melt. Therefore, at longer distances, the degree of particle oxidation is significantly higher

than that at shorter distances. This oxide is distributed uniformly in the coating thereby increasing the hardness of the coating to a certain extent [33].

4. Conclusions

In this study, a stable laminar plasma jet with a length of above 600 mm was obtained. We prepared molybdenum coatings using laminar plasma spray at different spray distances and discussed the particle behaviors during the spraying process and the following conclusions were drawn:

1) Two types of oxidation occur during the laminar plasma spraying process: post-deposition oxidation and in-flight oxidation. Post-deposition oxidation occurs mainly when the spray distance is short, and in-flight oxidation is more severe when the spray distance is long.

2) All particles are sufficiently heated within the spray distance of 200 mm to 400 mm. Some particles, especially beyond 300 mm, are of lower temperature due to the evaporation of the volatile oxide but their temperature is still higher than the local melting point and therefore they remain in molten state.

3) Laminar plasma sprayed coatings show lamellar structure that hardly changes with the spray distance. The coatings obtained at all the five spray distances exhibit strong similarities.

4) The hardness of the coating is mainly dependent on the oxide content. When the spraying distance is longer, the in-flight oxidation of the particles is more severe, the hard oxide is more uniformly distributed in the coating, and the hardness of the coating is higher as compared to when the spray distance is shorter.

CRediT authorship contribution statement

Hui-Yu Zhang:Data curation, Writing - review & editing, Methodology.**Sen-Hui Liu**:Visualization, Investigation, Software.**Chang-Jiu Li**:Resources.**Cheng-Xin Li**:Supervision.

Declaration of competing interest

We declare that we have no financial and personal relationships with other people or organizations that can inappropriately influence our work. There is no professional or other personal interest of any nature or kind in any product, service and/or company that could be construed as influencing the position presented in the manuscript entitled “Deposition and Oxidation Behavior of Atmospheric Laminar Plasma Sprayed Mo Coatings from 200 mm to 400 mm under 20 kW: Numerical and Experimental Analyses”.

Acknowledgements

The authors are grateful to Mr. Jin-Xi Wang from Department of Materials Science and Engineering in Xi'an Jiaotong University for the help in preparation of specimens. This work was supported by the Natural Key R&D Program of China (Basic Research Project, Grant No. 91860114). And we would like to thank Editage (www.editage.cn) for English language editing.

Appendix A. Supplementary data

Supplementary data to this article can be found online at https://doi.org/10.1016/j.surfcoat.2020.126245.

References

[1] K. Yang, J. Rong, J. Feng, Y. Zhuang, H. Zhao, L. Wang, J. Ni, S. Tao, F. Shao, C. Ding, Excellent wear resistance of plasma-sprayed amorphous Al2O3–Y3Al5O12 ceramic coating, Surf. Coatings Technol. 326 (2017) 96–102, https://doi.org/10.1016/j.surfcoat.2017.07.038.

[2] N.P. Padture, M. Gell, E.H. Jordan, Thermal barrier coatings for gas-turbine engine applications, Science 296 (2002) 280–284, https://doi.org/10.1126/science.1068609.

[3] J. Li, C.X. Li, G.J. Yang, C.J. Li, Effect of vapor deposition in shrouded plasma spraying on morphology and wettability of the metallic Ni20Cr coating surface, J. Alloys Compd. 735 (2018) 430–440, https://doi.org/10.1016/j.jallcom.2017.11.135.

[4] L.S. Wang, C.X. Li, C.J. Li, G.J. Yang, Performance of La0.8Sr0.2Ga0.8Mg0.2O3-based SOFCs with atmospheric plasma sprayed La-doped CeO2 buffer layer, Electrochim. Acta 275 (2018) 208–217, https://doi.org/10.1016/j.electacta.2018.04.101.

[5] Y.Z. Hu, Y.T. Su, C.X. Li, C.J. Li, G.J. Yang, Dense Mn1.5Co1.5O4 coatings with excellent long-term stability and electrical performance under the SOFC cathode environment, Appl. Surf. Sci. 499 (2020) 143726, , https://doi.org/10.1016/j.apsusc.2019.143726.

[6] S. Prakash, W.A. Sirignano, Liquid fuel droplet heating with internal circulation, Int. J. Heat Mass Transf. 21 (1978) 885–895, https://doi.org/10.1016/0017-9310(78)90180-1.

[7] X. Cao, D. Yu, M. Xiao, J. Miao, Y. Xiang, J. Yao, Design and characteristics of a laminar plasma torch for materials processing, Plasma Chem. Plasma Process. 36 (2016) 693–710, https://doi.org/10.1007/s11090-015-9661-6.

[8] K. Osaki, O. Fukumasa, A. Kobayashi, High thermal efficiency-type laminar plasma jet generator for plasma processing, Vacuum 59 (2000) 47–54, https://doi.org/10.1016/S0042-207X(00)00253-0.

[9] W. Pan, W. Zhang, W. Zhang, C. Wu, Generation of long, laminar plasma jets at atmospheric pressure and effects of flow turbulence, Plasma Chem. Plasma Process. 21 (2001) 23–35, https://doi.org/10.1023/A:1007037327834.

[10] Y. Xiang, D. Yu, Q. Li, H. Peng, X. Cao, J. Yao, Effects of thermal plasma jet heat flux characteristics on surface hardening, J. Mater. Process. Technol. 226 (2015) 238–246, https://doi.org/10.1016/j.jmatprotec.2015.07.022.

[11] X. Cao, D. Yu, Y. Xiang, J. Yao, J. Miao, Influence of the laminar plasma torch construction on the jet characteristics, Plasma Sci. Technol. 18 (2016) 740–743, https://doi.org/10.1088/1009-0630/18/7/07.

[12] H.Y. Zhang, C.X. Li, S.H. Liu, L. Li, G.J. Yang, C.J. Li, S.L. Zhang, Splash involved deposition behavior and erosion mechanism of long laminar plasma sprayed NiCrBSi coatings, Surf. Coatings Technol. 395 (2020), https://doi.org/10.1016/j.surfcoat.2020.125939.

[13] S.H. Liu, S.L. Zhang, C.X. Li, L. Li, J.H. Huang, J.P. Trelles, A.B. Murphy, C.J. Li, Generation of long laminar plasma jets: experimental and numerical analyses, Plasma Chem. Plasma Process. 39 (2019) 377–394, https://doi.org/10.1007/s11090-018-9949-4.

[14] S.H. Liu, C.X. Li, L. Li, J.H. Huang, P. Xu, Y.Z. Hu, G.J. Yang, C.J. Li, Development of long laminar plasma jet on thermal spraying process: microstructures of zirconia coatings, Surf. Coatings Technol. 337 (2018) 241–249, https://doi.org/10.1016/j.surfcoat.2018.01.003.

[15] S.H. Liu, C.X. Li, H.Y. Zhang, S.L. Zhang, L. Li, P. Xu, G.J. Yang, C.J. Li, A novel structure of YSZ coatings by atmospheric laminar plasma spraying technology, Scr. Mater. 153 (2018) 73–76, https://doi.org/10.1016/j.scriptamat.2018.04.022.

[16] B. Hwang, S. Lee, J. Ahn, Correlation of microstructure and wear resistance of molybdenum blend coatings fabricated by atmospheric plasma spraying, Mater. Sci. Eng. A 366 (2004) 152–163, https://doi.org/10.1016/j.msea.2003.09.062.

[17] van Sanden, R. Severens, J. Bastiaanssen, D. Schram, J. Bastiaanssen, High-quality a-Si:H growth at high rate using an expanding thermal plasma, Surf. Coatings Technol. 97 (1997) 719–722, https://doi.org/10.1016/S0257-8972.

[18] H.H. Xi, P.F. He, H.D. Wang, M. Liu, S.Y. Chen, Z.G. Xing, G.Z. Ma, Z.L. Lv, Microstructure and mechanical properties of Mo coating deposited by supersonic plasma spraying, Int. J. Refract. Met. Hard Mater. 86 (2020) 105095, https://doi.org/10.1016/j.ijrmhm.2019.105095.

[19] S.H. Liu, J.P. Trelles, A.B. Murphy, L. Li, S.L. Zhang, G.J. Yang, C.X. Li, C.J. Li, Numerical simulation of the flow characteristics inside a novel plasma spray torch, J. Phys. D. Appl. Phys. 52 (2019), https://doi.org/10.1088/1361-6463/ab228b.

[20] D.P. Guillen, B.G. Williams, In-flight oxidation of aluminum in the twin-wire electric arc process, J. Therm. Spray Technol. 15 (2006) 63–71, https://doi.org/10.1361/105996306X92604.

[21] A.A. Syed, A. Denoirjean, P. Fauchais, J.C. Labbe, On the oxidation of stainless steel particles in the plasma jet, Surf. Coatings Technol. 200 (2006) 4368–4382, https://doi.org/10.1016/j.surfcoat.2005.02.156.

[22] G. Espie, A. Denoirjean, P. Fauchais, J.C. Labbe, J. Dubsky, O. Schneeweiss, K. Volenik, In-flight oxidation of iron particles sprayed using gas and water stabilized plasma torch, Surf. Coatings Technol. 195 (2005) 17–28, https://doi.org/10.1016/j.surfcoat.2004.05.030.

[23] V.V. Sobolev, J.M. Guilemany, Influence of oxidation on coating formation in thermal spraying, J. Mater. Process. Manuf. Sci. 7 (1999) 271–286, https://doi.org/10.1106/9ERD-WRT3-YUVD-HC9K.

[24] C.J. Li, J.L. Li, Evaporated-gas-induced splashing model for splat formation during plasma spraying, Surf. Coatings Technol. 184 (2004) 13–23, https://doi.org/10.1016/j.surfcoat.2003.10.048.

[25] C.J. Li, C.X. Li, G.J. Yang, Y.Y. Wang, Examination of substrate surface melting-induced splashing during splat formation in plasma spraying, Proc. Int. Therm. Spray Conf, 2006, pp. 717–724, , https://doi.org/10.1361/105996306X146947.

[26] H.X. Wang, X. Chen, W. Pan, Effects of the length of a cylindrical solid shield on the entrainment of ambient air into turbulent and laminar impinging argon plasma jets, Plasma Chem. Plasma Process. 28 (2008) 85–105, https://doi.org/10.1007/s11090-007-9109-8.

[27] O. Racek, The effect of HVOF particle-substrate interactions on local variations in the coating microstructure and the corrosion resistance, J. Therm. Spray Technol.

19 (2010) 841–851, https://doi.org/10.1007/s11666-010-9483-2.
[28] S. Chandra, P. Fauchais, Formation of solid splats during thermal spray deposition, J. Therm. Spray Technol. 18 (2009) 148–180, https://doi.org/10.1007/s11666-009-9294-5.
[29] G.R. Li, H. Xie, G.J. Yang, Scale-progressive healing mechanism dominating the ultrafast initial sintering kinetics of plasma-sprayed thermal barrier coatings, Ceram. Int. 44 (2018) 16732–16738, https://doi.org/10.1016/j.ceramint.2018.06.102.
[30] G. Li, G. Yang, Understanding of degradation-resistant behavior of nanostructured thermal barrier coatings with bimodal structure, J. Mater. Sci. Technol. 35 (2019) 231–238, https://doi.org/10.1016/j.jmst.2018.09.054.
[31] G. Jin, B. shi Xu, H. Dou Wang, Q. Fen Li, S. Cheng Wei, Tribological properties of molybdenum coatings sprayed by electro-thermal explosion directional spraying, Surf. Coatings Technol. 201 (2007) 6678–6680, https://doi.org/10.1016/j.surfcoat.2006.09.028.
[32] W.X. Pan, X. Meng, G. Li, Q.X. Fei, C.K. Wu, Feasibility of laminar plasma-jet hardening of cast iron surface, Surf. Coatings Technol. 197 (2005) 345–350, https://doi.org/10.1016/j.surfcoat.2004.06.043.
[33] J.R. Davis, Handbook of Thermal Spray Technology, A, ASM International, 2004.